Magnetic proximity-induced energy gap of topological surface states

Jiashu Wang,[1] Tianyi Wang,[1] Mykhaylo Ozerov,[2] Zhan Zhang,[3] Seul-Ki Bac,[1] Hoai Trinh,[1] Maksym Zhukovskyi,[4] Tatyana Orlova,[4] Haile Ambaye,[5] Jong Keum,[5,6] Dmitry Smirnov,[2] Valeria Lauter,[5] Xinyu Liu,[1] Badih A. Assaf[1]

[1] Department of Physics and Astronomy, University of Notre Dame, Notre Dame IN, 46556, USA

[2] National High Magnetic Fields Laboratory, Florida State University, Tallahassee, FL, 32310, USA

[3] X-ray Science Division, Advanced Photon Source, Argonne National Lab, Lemont, IL, 60439, USA

[4] Notre Dame Integrated Imaging Facility, University of Notre Dame, Notre Dame IN, 46556, USA

[5] Neutron Scattering Division, Neutron Sciences Directorate, Oak Ridge National Laboratory, Oak Ridge, TN 37831, USA

[6] Center for Nanophase Materials Sciences, Physical Science Directorate, Oak Ridge National Laboratory, Oak Ridge, Tennessee 37831, USA

Abstract. Topological crystalline insulator surface states can acquire an energy gap when time reversal symmetry is broken by interfacing with a magnetic insulator. Such hybrid topological-magnetic insulator structures can be used to generate novel anomalous Hall effects and to control the magnetic state of the insulator in a spintronic device. In this work, the energy gap of topological surface states in proximity with a magnetic insulator is measured using Landau level spectroscopy. The measurements are carried out on $Pb_{1-x}Sn_xSe$ – EuSe heterostructures grown by molecular beam epitaxy exhibiting record mobility and a low Fermi energy enabling this measurement. We find an energy gap that does not exceed 20meV and we show that is due to the combined effect of quantum confinement and magnetic proximity. The presence of magnetism at the interface is confirmed by magnetometry and neutron reflectivity. The recovered energy gap sets an upper limit for the Fermi level needed to observe the quantized anomalous Hall effect using magnetic proximity heterostructures.

Introduction

Topological insulators are materials that host gapless Dirac surface states due to a band inversion at high symmetry points in momentum space.[1,2] Charge carriers occupying these states have their spin degree of freedom locked to the momentum thus enabling spin-charge conversion. When these topological Dirac states are in proximity with magnetism, they acquire an energy gap due to broken time-reversal symmetry as illustrated in Fig. 1(a).[1,3,4] TI – magnetic insulator heterostructures are being pursued both for spintronic device applications [5,6,7,8,9] and to realize new quantum effects with broken time-reversal symmetry. The study of these heterostructures has thus been a consistent topic of interest both for applications and fundamental physics.

Fundamentally, the magnetic proximity effect is a route to introduce magnetism onto various states of matter without chemical doping.[1,3,10,11,12,13] It is being pursued in TIs for the realization of the quantized anomalous Hall effect (QAHE)[10] which requires topological surface state to have a large energy gap larger. In topological crystalline insulators which are TIs with valley degenerate surface states protected by mirror symmetry, the QAHE effect has not yet been achieved, but has been predicted to be larger than for TIs and tunable.[14]

Several experiments have studied the electrical and magnetic properties of heterostructures of TI and a magnetic insulator (MI), but the electronic structure and energy gap of topological surface states in proximity with magnetism have yet to be measured.[3,15,16,17,18,19,20,21,22] A knowledge of the size of this gap is important as it provides as a metric of the strength of the magnetic proximity effect. The exact nature of spin-momentum locking in the presence of time reversal symmetry breaking also depends on the size of this energy gap.[23,24] Its measurement in the presence of a magnetic proximity with an insulator is thus important for spintronic devices. This measurement has not yet been done partly because most tools utilized to probe band structure are surface sensitive and cannot probe states located below a nanometer-thick MI layer. We will refer to states located at the TI/MI interface as topological interface states (TIS) in the remainder of this work. The mechanism by which the MI interacts with an underlying TIS remains unclear and controversial.[25,26] A measurement of the energy gap of the TIS can also shed light on this problem.

Here, we report a measurement of this energy gap E_{TIS} when the TIS of a topological crystalline insulator are in proximity to an MI, in $Pb_{1-x}Sn_xSe$-EuSe heterostructure grown by molecular beam epitaxy (MBE) and sketched in Fig. 1(b). Magnetooptical Landau level spectroscopy allows us to measure E_{TIS}=14±6meV when the topological states are in proximity with magnetism. Polarized neutron reflectometry (PNR) and SQUID magnetometry measurements demonstrate that the alternating EuSe layers are in a fully saturated ferromagnetic state in proximity to the TIS at low temperature and high magnetic field. The origin of E_{TIS} in our experiment is shown to be due to the combined effect of time-reversal symmetry breaking and magnetism. Our work thus establishes a previously unknown upper limit on the TIS gap due to the magnetic proximity effect. Importantly, we find that in $Pb_{1-x}Sn_xSe$-EuSe, the Fermi energy is only 40meV above the middle

of E_{TIS} demonstrating the potential of topological crystalline insulators as high-quality alternatives for the realization of TI-MI devices.

Our material of choice $Pb_{1-x}Sn_xSe$ is a tunable topological crystalline insulator with degenerate surface states that are protected by mirror symmetry and time reversal symmetry.[27,28] It is ideal to test the proximity effect since it has a crystal structure identical to Eu-chalcogenides, commonly used in magnetic proximity effect devices.[3,29] Thus, It can be epitaxially matched to them without impacting sample quality.[30,31,32] This fact allows the proximity-induced gap of the TIS to be measured using Landau level spectroscopy. This method is a highly reliable tool for measuring narrow energy gaps[33,34,35,36] and for characterizing semimetals.[37,38,39] The $Pb_{1-x}Sn_xSe$-EuSe interface and our heterostructures also host a quasi-type-I band alignment with a band inversion and ensures that inversion symmetry is preserved.

Results.

Structural properties of the heterostructures

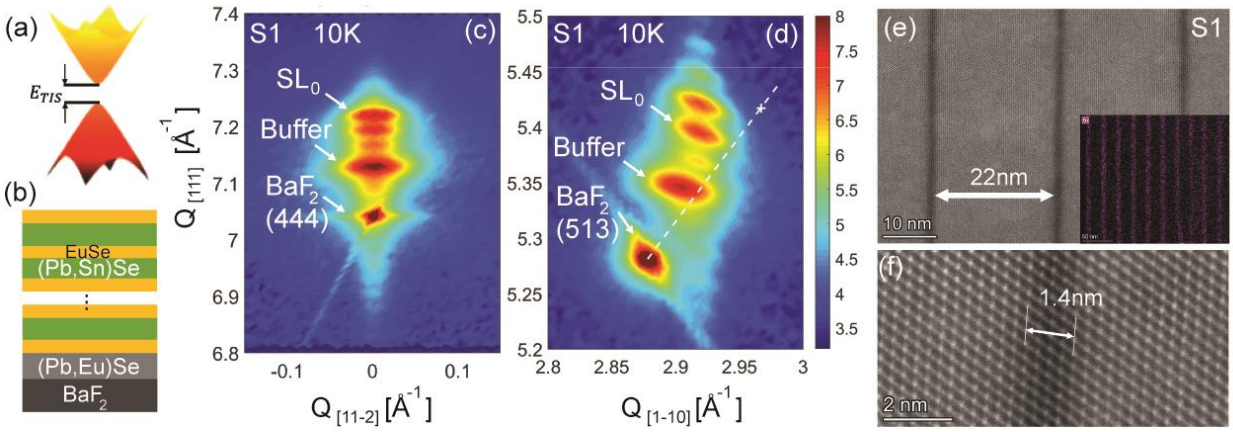

FIG 1. Crystal structure of sample S1. (a) Sketch of the massive Dirac dispersion of topological interface states after gap opening. (b) Diagram of the sample structure. The EuSe/$Pb_{1-x}Sn_xSe$/EuSe structure is repeated 5 or 10 times. (c) Reciprocal space map (RSM) taken on sample S1 showing the (444) Bragg peak of the BaF_2 substrate, the $Pb_{1-y}Eu_ySe$ buffer layer and the $Pb_{1-x}Sn_xse$/EuSe superlattice (SL). (d) Reciprocal space map of the (513) Brag reflection taken on S1. RSMs are taken at T=10K. (e) TEM image of a few wells from samples S1. Bottom right inset: EDX image of Eu distribution taken across all 10 periods of sample S1. (f) Zoom-in at the interface between $Pb_{1-x}Sn_xSe$ (light) and the EuSe barrier (dark).

The $Pb_{1-x}Sn_xSe$/EuSe superlattices oriented in the (111) direction are grown on BaF_2 (111) substrates by MBE. First, a thick buffer layer of insulating $Pb_{0.84}Eu_{0.16}Se$ (400-500nm) is grown to reduce the lattice mismatch between the $Pb_{1-x}Sn_xSe$ wells (a=6.107-6.088Å) and the substrate (a=6.196Å). Above the buffer layer we grow a periodic stack of $Pb_{1-x}Sn_xSe$/EuSe multiquantum wells. We study 5 samples listed in table 1. Two samples N1 and N2 are dedicated to neutron reflectivity measurements. we focus on samples S1 and N1 in the manuscript.

X-ray diffraction (XRD) carried out at T=10K, allow us to extract the strain state of S1 at temperatures of interest. In Fig. 1(c), a reciprocal space map (RSM) taken along (444) at T=10K shows the Bragg peaks of the substrate, the (Pb,Eu)Se buffer layer and the $Pb_{1-x}Sn_xSe$ well for sample S1. Periodic peaks from the superlattice structure are also resolved indicating a highly coherent heterostructure. The patterns allow us to extract the superlattice period for each sample. This is consistently checked with transmission electron microscopy (TEM) measurements and X-ray reflectometry (XRR) (see supplementary section 1) to extract the well and EuSe thickness separately. The structural properties of the samples are shown in Table 1. In Fig. 1(d), an RSM along (513) allows us to compute the in-plane and out-of-plane lattice constant and extract information about the strain. The superlattice is under tensile strain in the in-plane direction and compressive strain in the [111] direction.

Transmission electron microscopy images confirm the observations of XRD. Fig. 1(e) shows a well-aligned stack of $Pb_{1-x}Sn_xSe$ and EuSe probed using TEM in sample S1. The inset of this image displays an elemental mapping of the Eu atom using energy dispersive X-ray spectroscopy that demonstrates the periodic repetition of the EuSe layers. A zoom-in figure (Fig. 1(f)) shows an interface between the well and the barrier demonstrating a short-range roughness of about a monolayer. We highlight that samples with thicker EuSe layers (>3nm) yielded rougher interfaces, therefore we restrict this analysis to thinner layers. Additional XRD, XRR and TEM measurements are included in supplementary section 1. The large gap of EuSe (>1eV) prohibits interactions between neighboring quantum wells, so the heterostructure can be safely considered as a multi-quantum well (see supplementary section 2).[32]

Sample	Sn concentration x	$Pb_{1-x}Sn_xSe$ Well thickness(nm)	EuSe Barrier thickness(nm)	No. of periods
S1	0.28 by EDX	22(±1)	1.41±0.35 (4±1ML)	10
S2	0.34 by XRD	25(±2)	2.4	5
S3	0.14 by XRD	32	6	5
N1	0.10 by XRD	48	11	5
N2	0.22 by XRD	35	4±2, varies by layer	5

Table 1. Sample list. The Sn concentration is determined using energy dispersive spectroscopy performed during the TEM measurements and X-ray diffraction on controlled bulk samples. The well and barrier thickness are extracted from a period determined by X-ray diffraction of the superlattice and cross-section TEM measurements. The uncertainty accounts for the interface roughness. X-ray diffraction patterns for all samples are shown in Supplementary section 1.

Magnetooptical measurements

We employ magneto-optical infrared spectroscopy to probe the energy gap of the TIS in proximity to EuSe. Experiments are performed in applied magnetic fields up to 17.5T using transmission and reflection measurements (Fig. 2(a)). The transmission spectra revealed a very weak signal between 25 and 72 meV corresponding to the reststrahlen band of the BaF_2 substrate. Therefore, we employed the reflection geometry to study the infrared signal from the

heterostructure in this spectral range. In the presence of a magnetic field, infrared excites transitions between various Landau levels (LLs) as illustrated in Fig. 2(b). The minima in the normalized transmission spectra T(B)/T(B=0) allow us to extract the energy of these transitions.

The experimental spectra obtained using transmission measurements are shown in Fig. 2(c) for S1. Owing to the high mobility of the TIS in $Pb_{1-x}Sn_xSe$, LL transitions that shift to higher energy as the field increases can be observed at fields as low as 3T. Some are marked with blue and gray dots to highlight the field dependence. Color coding will become clear later.

To obtain information about the transitions occurring in the reststrahlen of the substrate, we carried out reflectivity measurements in the far-infrared. The relative reflectance is shown in Fig. 2(d). Below 75meV, reflectance is strong, and a prominent minimum marked with a black square is observed. Other field-independent modulations of the reflectivity are ignored, since they cannot be related to LLs and are of no interest for our analysis.

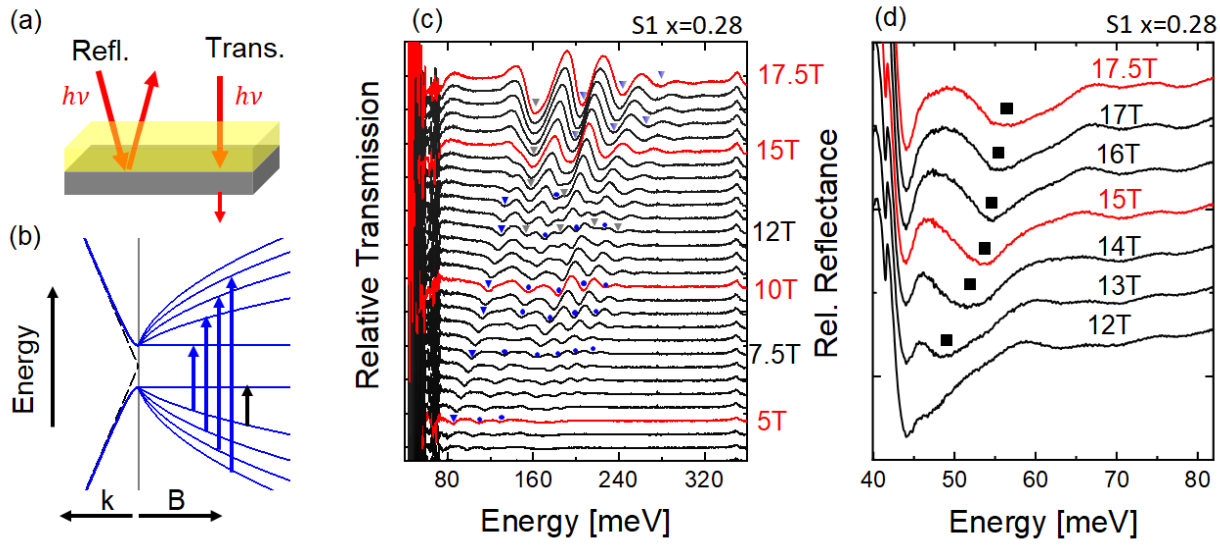

FIG 2. Magnetooptical measurements taken on S1. Landau level spectroscopy setup in the (a) transmission and reflection geometry. Reflectance is carried out in the reststrahlen band of the substrate. (b) Band dispersion and LLs of gapped TIS versus wavenumber k and versus magnetic field B. Blue arrows represent interband Landau level transitions and the black arrow is the cyclotron resonance (CR) (c) Relative magnetooptical transmission spectra (T(B)/T(0)) measured between 4T and 17.5T on S1. (d) Relative reflectance spectra (T(B)/T(0)) measured between 12T and 17.5T on S1. All measurements are made at 4.5K. The CR is marked with the black square, the structure of peaks and troughs near 40meV is due to a BaF_2 phonon.

We identify all transitions observed as minima in Fig. 2(c,d) by points presented in Fig. 3(a). Those transitions are shown in the empirical LL graphs plotted in Fig. 3(b). By modelling these LL transitions using a massive Dirac Hamiltonian[30] we can determine their origin. The transitions marked in blue in Fig. 2(c) and Fig. 3(a) are due to interband transitions between the conduction and valence LLs of the TIS. The intraband band transition between the 0^{th} and the 1^{st} LL is shown

by the black square. Those marked in gray are associated with interband transitions from the LLs of trivial quantum well subbands. We make this attribution following analysis using the semi-empirical model discussed next.

Fig. 3(a) shows a curve fit carried out using the following relation which describes interband magnetooptical transitions for massive Dirac fermions given dipole selection rules [4041] (see supplementary section 2):

$$\epsilon_n^{E,i} - \epsilon_{n\pm1}^{H,i} = \sqrt{\Delta_i^2 + 2ev^2\hbar^2 nB} + \sqrt{\Delta_i^2 + 2ev^2\hbar^2 (n \pm 1)B}$$

Here Δ_i the band edge position of each subband, *i* is the subband index (*i=1 for the TIS*), E/H denote the conduction and valence subbands respectively, v is the band velocity taken to be the same for all subbands, n is the Landau index, and *B* is the magnetic field. $\epsilon_n^{E,i}$ thus denotes the energy of the nth LL of the ith electron subband. A k.p formalism using the envelope function scheme allows us to derive the band dispersion to show that it indeed satisfies this quasi-ideal massive Dirac model (see supplementary material).[30,42] The solid blue lines in Fig. 3(a) represent transitions obtained from Eq. (1) for the TIS and the gray lines represent those from trivial QW subbands. Their extrapolation to B=0 yields the gap between each pair of conduction and valence subbands with the same index *i (i.e.* $2\Delta_i$ the gap between E_i and H_i*)*. $2\Delta_1$ is E_{TIS}. It is zero for a thick quantum well and if time-reversal symmetry is preserved. The corresponding LLs for all subbands up to i=3 are shown in Fig. 3(b) with the transitions shown as arrows.

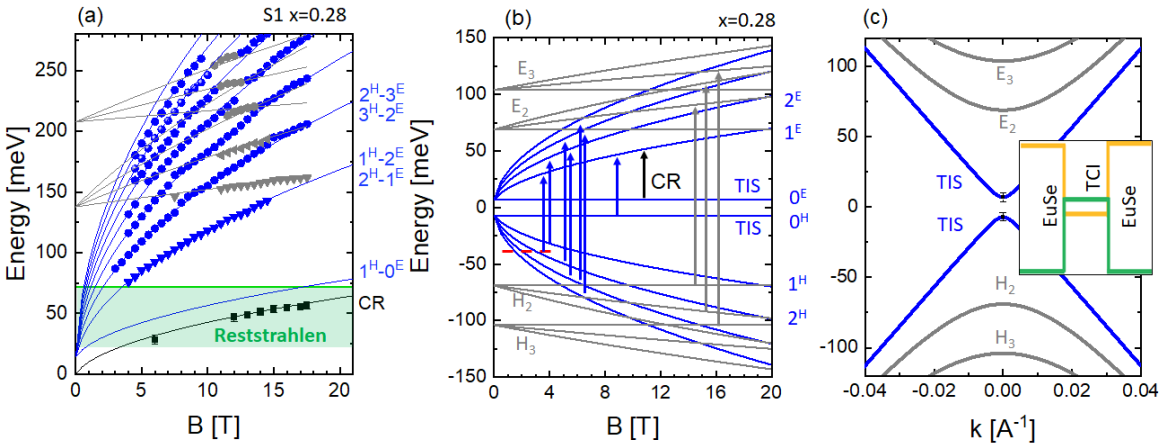

FIG 3. **Landau levels of sample S1 EuSe-$Pb_{0.72}Sn_{0.28}$Se-EuSe**. (a) Fan chart extracted from the experimental measurements and compared to the empirical model. Blue points represent the interband transitions of the TIS, the gray points represent those of QW subbands E_i and H_i (i>2) and the black points represent the CR of the TIS. The solid lines are the calculated transitions. They follow the same color scheme. (b) Landau levels of $Pb_{0.72}Sn_{0.28}$Se-EuSe utilized to compute the transitions shown in (a). The numbers on the left ($n^{E/VH}$) label the conduction and valence Landau levels of the TIS. The dashed red line marks the position of the Fermi energy. (c) Band dispersion of $Pb_{0.72}Sn_{0.28}$Se-EuSe obtained from the experiment. The uncertainty

on the TIS energy gap is shown at the band edge. The inset shows the band alignment and the topological states peaked at the interface.

The cyclotron resonance (CR) corresponds to the intraband transition between the valence n=0 and n=1 levels of the TIS, whose energy is given by:

$$\epsilon_{CR} = \sqrt{\Delta_1^2 + 2ev^2\hbar^2 nB} - \Delta_1$$

This transition is shown as the black line in Fig. 3(a) and the black arrow in Fig. 3(b). The fit to the interband transitions and the CR in Fig. 3(a) yield the following gaps: the TIS gap $E_{TIS} = 2\Delta_1 = 14 \pm 6meV$, the gap between E_2 and H_2 $2\Delta_2 = 68 \pm 2meV$, and between E_3 and H_3 $2\Delta_2 = 204 \pm 2meV$. The Fermi energy can also be determined from to be 40meV from the field at which the 3-4 transition disappears as the n=3 LL crosses the Fermi level (Fig. 3(a,b)). This experimental measurement allows us to reconstruct the band dispersion (in the QW plane) shown in Fig. 3(c). Despite the presence of the EuSe layer, the TIS gap cannot exceed 20meV within one standard deviation. The fit also yields the velocity $v = 4.3 \pm 0.05 \times 10^5 m/s$. Since we observe several transitions, our uncertainty on v and Δ_i is very small. Data taken on sample S2 is presented in the supplement and yields similar but less precise results as its mobility was lower.

The experimental results for both samples S1 and S2 are shown in Table 2. The extracted energy gaps are compared to a theoretical calculation carried out to determine the impact of only quantum confinment and strain on the trivial and topological states (supplementary sections 2 and 3). It utilizes the band alignment shown in Fig. 3(c), and is further discussed in the supplement. The resulting gaps are also shown in Table 2. The TIS gap from the experiment is only slightly larger than the theoretical value calculated without including magnetic exchange.

Sample ID	$E_{TIS} = 2\Delta_1$ (meV)	E2-H2 gap $2\Delta_2$	E3-H3 gap $2\Delta_3$
S1 – Exp.	14±6	136(±4) meV	206 meV
S1 – Cal.	7	129 meV	204 meV
S1 – Cal. with strain	10	122 meV	198 meV
S2 – Exp.	10±10meV	N/A	N/A
S2 – Calc.	2meV	141meV	201meV

Table 2. Experimental and theoretical energy gaps for S1 and S2. The calculation utilizes an envelope function scheme implemented using the band alignment shown in the inset of Fig. 3(c) and discussed in the supplementary section 2. Magnetic exchange is neglected in these calculations. The measurements for S2 are shown in supplementary section 4.

Magnetic measurements.

We have performed SQUID magnetization measurements to identify the magnetic phases of our EuSe barriers. Fig. 4(a) shows the magnetic moment versus temperature with B=100G applied parallel to the sample surface. The curve consists of two main contributions: the paramagnetic signal (PM) of the $Pb_{1-x}Eu_xSe$ buffer layer, which increases as the temperature decreases

following the Curie law and the antiferromagnetic signal from the EuSe barriers, which yields a peak at the Néel temperature. All curves shown in Fig. 4(a) exhibit such a peak, indicating AFM order from the EuSe barriers. The extracted Néel temperature T_N is plotted in Fig. 4(b). It increases with Sn concentration. This is likely due to the strain caused by a change in the lattice parameter of the $Pb_{1-x}Sn_xSe$ layer with increasing x.[43] The field-dependent magnetization was also measured and shown in Fig. 4(c) for the three samples considered here at 2K. Based on the estimated thickness we have calculated the average magnetic moment $\overline{m}_{Eu}$ per Eu^{2+} in Fig. 4(c) after the correction for diamagnetism of the BaF_2 substrate and the PM of the buffer layer (see supplementary section 5). The fine structure of the magnetization versus magnetic field – reflecting transitions from an AFM ground state to an FiM phase and finally to a saturated state – is only visible for samples with a thick EuSe layer ($\geq 4nm$). But, the magnetic moment saturates to a value close to the expected saturation from Eu^{2+} ions, $7\mu_B/Eu^{2+}$. Thus, for magnetic fields at which optical measurements are carried out, the moment of the EuSe layers can be considered saturated, and the extrapolation of the LLs to B=0 should yield E_{TIS} in the presence of a ferromagnet in proximity.

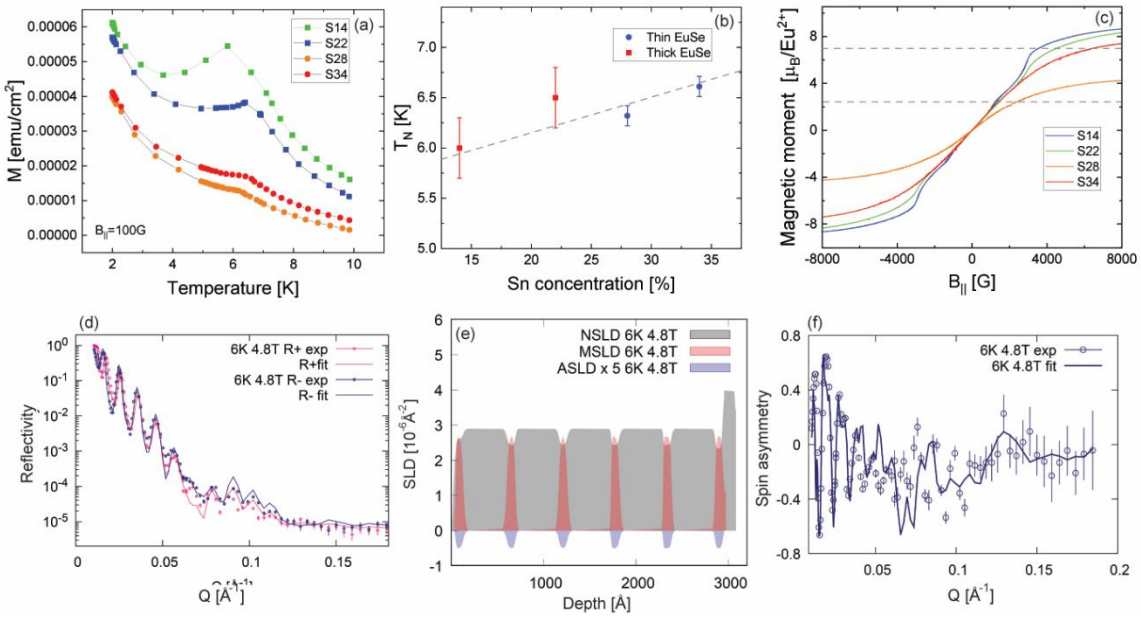

Figure 4. Magnetic properties and polarized neutron reflectivity measurements. (a) Magnetization versus temperature at 0.01T for 4 samples with different Sn concentrations. (b) The Neel temperature extracted from (a) for each sample plotted versus Sn concentration. (c) Magnetization versus magnetic field for samples with different Sn content. The dashed lines indicate the expected magnetic moment per Eu^{2+} in FiM and FM states of EuSe. (d) Measured (symbols) and fitted (solid lines) reflectivity curves for spin-up (R_+) and spin-down (R_-) neutron spin-states as a function of wavevector transfer Q = 4πsin(θ)/λ, where θ is the incident angle and λ is the neutron wavelength. (e) PNR nuclear (NSLD, in grey), magnetic (MSLD, in pink) and absorption (ASLD, in blue) scattering length density profiles, measured 6 K with an external in-

plane magnetic field of 4.5 T and presented as a function of depth. The finite ASLD is due to the presence of absorbing Eu atoms.[44] (f) The spin asymmetry ratio, $SA = (R_+ - R_-)/(R_+ + R_-)$, obtained from the experimental and fitted reflectivity data in (d).

To probe the depth profile of the magnetism at buried interfaces, we carried out PNR measurements on two samples (N1 and N2) at Oak Ridge National Lab. Data for N1 is shown in Figure 4 and N2 is discussed in supplementary section 6. The PNR measurements yield the spin resolved reflectivities R_+ and R_- as a function of the wavevector transfer Q at a fixed magnetic field (Fig. 4(d)). Superscripts plus (or minus) denote measurements with neutrons with spin parallel (or antiparallel) to the direction of the applied magnetic field. The depth profiles of the nuclear and magnetic scattering length densities (NSLD and MSLD) correspond to the depth profile of the chemical and in-plane magnetization vector distributions, respectively. Both are extracted using the fit shown in Fig. 4(d) and plotted in Fig. 4(e). Fig. 4(f) shows the spin asymmetry ratio $SA = (R_+ - R_-)/(R_+ + R_-)$ obtained from the experimental and fitted curves at ±4.85T. The SA signal evidences the presence of a depth dependent magnetic moment. The simulated depth profile in Fig. 4(e) and the SA in Fig. 4(f) confirm that we successfully obtain the intended periodic repetition of magnetic layers in proximity to every $Pb_{1-x}Sn_xSe$ layer. The peak MSLD signal is nearly constant in each of the 7 layers and converts to a value close to $5.5\mu_B/Eu^{2+}$ slightly lower than the value recovered from magnetometry. Despite the interface being atomically sharp at the nm scale, some roughness can be resolved in TEM measurements at the μm scale. This can cause a slight reduction of the magnetic moment probed by PNR.

Discussion.

We have thus extracted E_{TIS} for topological states in proximity to a magnetic insulator that achieve record mobility (see supplementary section 7). We focus the discussion on the origin of this gap as it can be due to time-reversal symmetry breaking or the hybridization of the top and bottom TIS. Comparison with theoretical calculations based on the envelop function method sheds light on this origin. Using the known bulk band parameters of $Pb_{1-x}Sn_xSe$ with x=0.28,[35] we compute the energy levels of S1 in the presence of quantum confiment and hybridization from the top and bottom surfaces. We neglect the effect of magnetism (see supplementary section 2). We can refine our model, by including the impact of in-plane tensile strain on the energy levels (see supplementary section 3). The strain parameters derived from (513) RSMs at T=10K reveal the impact of both lattice and thermal strain. For S1, this yields $\epsilon_{||} \approx +0.4\%$. Strain reduces the topological bulk gap of the $Pb_{0.72}Sn_{0.28}Se$, enhancing the hybridization gap of the TIS.[45][46][47] Results including and excluding the strain are shown in table 2. With the strain, we find a larger TIS hybridization gap that agrees with the experiment within the error but remains about 3meV below the result of the best fit. Thus, we can conclude that the TIS gap due to magnetism is equal to $4^{+6}_{-4} meV$ for S1. As a strict upper bound this gap cannot be larger than the upper bound of the experimetal gap E_{TIS} or 20meV. Sample S2 yields an identical upper bound.

While the magnetic proximity induced gap of the TIS has never been measured, it has been computed for the Bi_2Se_3/EuS interface. Previous ab-initio simulations on this type of structure have yielded a small magnetic Dirac gap close to 3meV for the interface, and 9meV for the top surface.[4] The small gap obtained for the EuS-Bi_2Se_3 interface is associated to the highly localized nature of the f-orbital in Eu. At that interface, evidence of charge transfer was observed in experiments[48] and ab-initio calculations[49]. In our system, charge transfer into the MI is unlikely since the two materials should have a type-I band alignment and since structure inherently preserves inversion symmetry. But, the scenario of orbital hybridization with the localized 4f level could also hold which can explain our result that the proximity induced gap is small.[4] This allows us to make an important conclusion. The magnetic proximity effect yields a narrow gap at the interface between a TCI and rare earth containing insulators. However, the low Fermi energy (40meV) recovered in our material motivates further studies on topological crystalline insulator – MI heterostructure which possess a high crystalline quality. A narrow gap is even advantageous for spintronic devices, since it is expected to preserve spin-momentum locking at the Fermi energy.[23]

Methods

MBE synthesis. The heterostructures are grown by molecular beam epitaxy on BaF_2(111) substrates. A compounds source of PbSe is utilized along with elemental sources of the following elements: Sn, Se, and Eu. A thick buffer layer of (Pb,Eu)Se (400-500nm) is initially grown to minimize dislocations in the heterostructures of interest. The buffer layer is followed by a EuSe/$Pb_{1-x}Sn_xSe$ heterostructure with either 5 or 10 periods. The thickness of the well is denoted by d and that of the barrier by d_B. They are controlled by the growth time. Thickness of the EuSe barrier differs for each sample but is kept larger than or equal to 1.1nm (3ML). The substrate temperature is fixed at 370°C during the growth and the Sn content x is varied by adjusting the relative flux between the PbSe cell and a Sn cell. A constant Se over-pressure is maintained throughout the growth. The well composition in each case is determined either by growing a control bulk epilayer of $Pb_{1-x}Sn_xSe$ (>200nm) under the same conditions and during the same run as the heterostructures and extracting its composition using X-ray diffraction, or by carrying out energy dispersive X-ray spectroscopy.

Magnetooptical measurements. Magneto-infrared experiments were performed using a commercial FT-IR spectrometer coupled with the vertical bore superconducting magnet at the National High Magnetic Fields Lab. The IR radiation propagates inside an evacuated metal tube from the spectrometer to the top of the magnet, whereas a brass light-pipe is used to guide the IR radiation down to the sample space. A parabolic cone was used to collect IR beam at the sample while two mirrors reflected the beam back up towards to the Si composite bolometer mounted just a short distance above the sample space. The sample is cooled down to 5 K using low pressure He exchange gas. The IR spectra were recorded in the mid-IR and far-IR range at fixed magnetic field, while field was stepped between 0 and 17.5T with increment of 0.5T. The reported spectra are obtained by dividing the signal at finite magnetic field by the zero-field spectrum.

Polarized Neutron Reflectometry. Polarized neutron reflectometry experiments were performed on the Magnetism Reflectometer at the Spallation Neutron Source at Oak Ridge National Laboratory,[50] using neutrons with wavelengths λ in a band of 2–8 Å and a high polarization of 98.5–99%. PNR is a highly penetrating depth-sensitive technique that can probe the chemical and magnetic depth profiles of

materials with a resolution of 0.5 nm. The depth profiles of the nuclear and magnetic scattering length densities (NSLD and MSLD) correspond to the depth profile of the chemical and in-plane magnetization vector distributions, respectively[51,52,53,54,55] Measurements were conducted in a closed cycle refrigerator equipped with a 5 T cryomagnet. Using the time-of-flight method, a collimated polychromatic beam of polarized neutrons with the wavelength band $\Delta\lambda$ impinges on the film at a grazing angle ϑ, interacting with atomic nuclei and the spins of unpaired electrons. The reflected intensity R_+ and R_- are measured as a function of wave vector momentum, $Q = 4\pi\sin(\theta)/\lambda$, with the neutron spin parallel (+) or antiparallel (–) to the applied field. To separate the nuclear from the magnetic scattering, the spin asymmetry ratio SA = $(R_+ - R_-)/(R_+ + R_-)$ is calculated, for which SA = 0 designating no magnetic moment in the system.

X-ray diffraction. X-ray diffraction measurements are carried out at room temperature in a Bruker D8 Discover diffractometer equipped with Cu-Kα-source. Low temperature X-ray diffraction measurements are carried out at beamline 33ID-D/E at the Advanced Photon Source at Argonne National lab using a wavelength of 0.61992Å.

SQUID magnetometry. SQUID magnetometry is carried out in a Quantum Design MPMS, down to 4.2 K at various magnetic fields up to 7 T. The field is applied parallel to the sample plane. The diamagnetism of the substrate measured at 2K is subtracted from magnetization versus field measurements. The paramagnetism of the buffer layer is accounted for by a saturating Brillouin function and can be differentiated from the intrinsic magnetic of the EuSe layer using the method discussion in the supplementary material.

Transmission electron microscopy. High-resolution cross-sectional TEM images were acquired using a double tilt holder and probe corrected Spectra 30-300 transmission electron microscope (Thermo Fisher Scientific, USA) equipped with a field emission gun, operated at 300 kV. STEM images were acquired using Panther STEM detector (Thermo Fisher Scientific, USA) in high-angle, annular dark field mode (HAADF) and bright field mode (BF). For compositional analysis, energy-dispersive X-ray spectroscopy (EDS) maps were obtained in STEM mode using the Super-X EDS system (Thermo Fisher Scientific, USA) equipped with 4 windowless silicon drift detectors. TEM samples were prepared by focused ion beam etching using the standard lift-out technique.

Theoretical Model. The band structure of the nontrivial $Pb_{1-x}Sn_xSe$ heterostructures can be theoretically calculated using an envelope function model developed in previous work (for details see supplementary section 1).[30,31] The model does not take magnetism into account and has been shown to agree with experiments when the barrier is a simple insulator with a large energy gap (1eV) without magnetic order.[30] The inverted band structure in the non-trivial $Pb_{1-x}Sn_xSe$ will lead to a confined topological interface state (TIS). The bulk bands of the system also yield trivial quantum well subbands. The dispersion of these bands is calculated by an empirical 4-band massive Dirac model:

$$\epsilon(k) = \pm\sqrt{(\Delta_i)^2 + \hbar^2 v^2 k^2}$$

Where Δ_i is the energy gap, v is the band velocity equal for the bulk and the confined system and k is the wavevector in the quantum well plane. The LLs of each band can be computed in a similar way:

$$\epsilon_n^{E/H}(B) = \pm\sqrt{(\Delta_i)^2 + 2ev^2\hbar nB}$$

In the magneto-optical measurment in the Faraday geometry, the selection rules require that electrons can only transition from n^H (the nth LL in valence band) to $(n \pm 1)^E$, and vice versa. Eq. (1) is derived with this in mind. More details concerning the model are given in the supplement.

Data availibity

The data that support the findings of this study are available from the corresponding author upon reasonable request.

1. Hasan, M. Z. & Kane, C. L. Colloquium: Topological insulators. *Rev. Mod. Phys.* **82**, 3045–3067 (2010).
2. Qi, X.-L. & Zhang, S.-C. Topological insulators and superconductors. *Rev. Mod. Phys.* **83**, 1057–1110 (2011).
3. Wei, P. *et al.* Exchange-Coupling-Induced Symmetry Breaking in Topological Insulators. *Phys. Rev. Lett.* **110**, 186807 (2013).
4. Lee, A. T., Han, M. J. & Park, K. Magnetic proximity effect and spin-orbital texture at the Bi2Se3/EuS interface. *Phys. Rev. B* **90**, 155103 (2014).
5. Mellnik, a. R. *et al.* Spin-transfer torque generated by a topological insulator. *Nature* **511**, 449–451 (2014).
6. Han, J. *et al.* Room-Temperature Spin-Orbit Torque Switching Induced by a Topological Insulator. *Phys. Rev. Lett.* **119**, 077702 (2017).
7. Fanchiang, Y. T. *et al.* Strongly exchange-coupled and surface-state-modulated magnetization dynamics in Bi2Se3/yttrium iron garnet heterostructures. *Nat. Commun.* **9**, (2018).
8. Li, P. *et al.* Magnetization switching using topological surface states. *Sci. Adv.* **5**, (2019).
9. Rojas-Sánchez, J.-C. *et al.* Spin to Charge Conversion at Room Temperature by Spin Pumping into a New Type of Topological Insulator: α-Sn Films. *Phys. Rev. Lett.* **116**, 096602 (2016).
10. Tokura, Y., Yasuda, K. & Tsukazaki, A. Magnetic topological insulators. *Nat. Rev. Phys.* **1**, 126–143 (2019).
11. Norden, T. *et al.* Giant valley splitting in monolayer WS2 by magnetic proximity effect. *Nat. Commun.* **10**, 4163 (2019).
12. Hauser, J. J. Magnetic proximity effect. *Phys. Rev.* **187**, 580–583 (1969).
13. Yao, X. *et al.* Record High-Proximity-Induced Anomalous Hall Effect in (BixSb1-x)2 Te2 Thin Film Grown on CrGeTe3 Substrate. *Nano Lett.* acs.nanolett.9b01495 (2019) doi:10.1021/acs.nanolett.9b01495.
14. Fang, C., Gilbert, M. J. & Bernevig, B. A. Large-chern-number quantum anomalous hall effect in thin-film topological crystalline insulators. *Phys. Rev. Lett.* **112**, 046801 (2014).

15. Katmis, F. *et al.* A high-temperature ferromagnetic topological insulating phase by proximity coupling. *Nature* **533**, 513–516 (2016).

16. Assaf, B. A. *et al.* Inducing magnetism onto the surface of a topological crystalline insulator. *Phys. Rev. B* **91**, 195310 (2015).

17. Kandala, a. *et al.* Growth and characterization of hybrid insulating ferromagnet-topological insulator heterostructure devices. *Appl. Phys. Lett.* **103**, 202409 (2013).

18. Yang, Q. I. *et al.* Emerging weak localization effects on a topological insulator–insulating ferromagnet (Bi_{2}Se_{3}-EuS) interface. *Phys. Rev. B* **88**, 081407 (2013).

19. Lang, M. *et al.* Proximity induced high-temperature magnetic order in topological insulator - ferrimagnetic insulator heterostructure. *Nano Lett.* **14**, 3459–65 (2014).

20. Riddiford, L. J. *et al.* Understanding Signatures of Emergent Magnetism in Topological Insulator/Ferrite Bilayers. *Phys. Rev. Lett.* **128**, 126802 (2022).

21. Grutter, A. J. & He, Q. L. Magnetic proximity effects in topological insulator heterostructures: Implementation and characterization. *Phys. Rev. Mater.* **5**, 090301 (2021).

22. He, Q. L. *et al.* Tailoring exchange couplings in magnetic topological-insulator/antiferromagnet heterostructures. *Nat. Mater.* **16**, 94–100 (2017).

23. Xu, S.-Y. *et al.* Hedgehog spin texture and Berry's phase tuning in a magnetic topological insulator. *Nat. Phys.* **8**, 616–622 (2012).

24. Lu, H.-Z., Zhao, A. & Shen, S.-Q. Quantum Transport in Magnetic Topological Insulator Thin Films. *Phys. Rev. Lett.* **111**, 146802 (2013).

25. Figueroa, A. I. *et al.* Absence of Magnetic Proximity Effect at the Interface of Bi2Se3 and (Bi,Sb)2Te3 with EuS. *Phys. Rev. Lett.* **125**, 226801 (2020).

26. Prokeš, K. *et al.* Search for enhanced magnetism at the interface between Bi2Se3 and EuSe. *Phys. Rev. B* **103**, 115438 (2021).

27. Hsieh, T. H. *et al.* Topological crystalline insulators in the SnTe material class. *Nat. Commun.* **3**, 982 (2012).

28. Hsieh, T. H. *et al.* Corrigendum: Topological crystalline insulators in the SnTe material class. *Nat. Commun.* **4**, 1901 (2013).

29. Krieger, J. A. *et al.* Do topology and ferromagnetism cooperate at the EuS/Bi2Se3 interface? *Phys. Rev. B* **99**, 1–10 (2019).

30. Krizman, G. *et al.* Tunable Dirac interface states in topological superlattices. *Phys. Rev. B* **98**, 075303 (2018).

31. Wang, J. *et al.* Weak antilocalization beyond the fully diffusive regime in Pb1-xSnxSe topological quantum wells. *Phys. Rev. B* **102**, 155307 (2020).

32. Krizman, G. *et al.* Miniband engineering and topological phase transitions in topological-insulator–normal-insulator superlattices. *Phys. Rev. B* **103**, 235302 (2021).

33. Jiang, Y. *et al.* Unraveling the Topological Phase of ZrTe5 via Magnetoinfrared Spectroscopy. *Phys. Rev. Lett.* **125**, 046403 (2020).

34. Jiang, Y. *et al.* Electron-Hole Asymmetry of Surface States in Topological Insulator Sb2Te3Thin Films Revealed by Magneto-Infrared Spectroscopy. *Nano Lett.* **20**, 4588–4593 (2020).

35. Krizman, G. *et al.* Dirac parameters and topological phase diagram of Pb1-xSnxSe from magnetospectroscopy. *Phys. Rev. B* **98**, 245202 (2018).

36. Teppe, F. *et al.* Temperature-driven massless Kane fermions in HgCdTe crystals. *Nat. Commun.* **7**, 12576 (2016).

37. Yuan, X. *et al.* The discovery of dynamic chiral anomaly in a Weyl semimetal NbAs. *Nat. Commun.* **11**, 1259 (2020).

38. Shao, Y. *et al.* Electronic correlations in nodal-line semimetals. *Nat. Phys.* **16**, 636–641 (2020).

39. Krizman, G. *et al.* Determination of the crystal field saplitting energy in Cd3As2 using magnetooptics. *Phys. Rev. B* **100**, 155205 (2019).

40. Bauer, G. Magnetooptical properties of IV–VI compounds. in *Narrow Gap Semiconductors Physics and Applications: Proceeding of the Internationl Summer School* (ed. Zawadzki, W.) vol. 133 427–446 (Springer Berlin Heidelberg, 1980).

41. Mitchell, D. L. & Wallis, R. F. Theoretical energy-band parameters for the lead salts. *Phys. Rev.* **151**, 581–595 (1966).

42. Bastard, G. *Wave mechanics applied to semiconductor heterostructures*. (1988).

43. Lechner, R. T. *et al.* Strain Induced Changes in the Magnetic Phase Diagram of Metamagnetic Heteroepitaxial EuSe / PbSe 1 − x Te x Multilayers. *Phys. Rev. Lett.* **94**, 157201 (2005).

44. Korneev, D. A., Pasyuk, V. V., Petrenko, A. V. & Jankovski, H. Absorbing sublayers and their influence on the polarizing efficiency of magnetic neutron mirrors. *Nucl. Instruments Methods Phys. Res. Sect. B Beam Interact. with Mater. Atoms* **63**, 328–332 (1992).

45. Zasavitskii, I. I., de Andrada e Silva, E. A., Abramof, E. & McCann, P. J. Optical deformation potentials for PbSe and PbTe. *Phys. Rev. B* **70**, 115302 (2004).

46. Simma, M., Fromherz, T., Bauer, G. & Springholz, G. Type I/type II band alignment transition in strained PbSe⁄PbEuSeTe multiquantum wells. *Appl. Phys. Lett.* **95**, 212103 (2009).

47. Simma, M., Bauer, G. & Springholz, G. Band alignments and strain effects in PbTe/Pb1-

xSrxTe and PbSe/Pb1-xSrxSe quantum-well heterostructures. *Phys. Rev. B* **90**, 195310 (2014).

48. Osterhoudt, G. B. *et al.* Charge transfer in heterostructures as indicated by the absence of Raman scattering. *Phys. Rev. B* **98**, 014308 (2018).

49. Tristant, D., Vekhter, I., Meunier, V. & Shelton, W. A. Partial charge transfer and absence of induced magnetization in EuS/Bi2Se3 heterostructures. *Phys. Rev. B* **104**, 075128 (2021).

50. Lauter, V., Ambaye, H., Goyette, R., Hal Lee, W. T. & Parizzi, A. Highlights from the magnetism reflectometer at the SNS. *Phys. B Condens. Matter* **404**, 2543–2546 (2009).

51. Lauter-Pasyuk, V. Neutron Grazing Incidence Techniques for Nano-science. *Collect. Soc. Fr. Neutron* **7**, s221–s240 (2007).

52. Blundell, S. J. *et al.* Spin-orientation dependence in neutron reflection from a single magnetic film. *Phys. Rev. B* **51**, 9395–9398 (1995).

53. Lauter-Pasyuk, V., Lauter, H. J., Toperverg, B. P., Romashev, L. & Ustinov, V. Transverse and Lateral Structure of the Spin-Flop Phase in Fe/Cr Antiferromagnetic Superlattices. *Phys. Rev. Lett.* **89**, 167203 (2002).

54. Lauter, H. *et al.* Domains and interface roughness in Fe/Cr multilayers: influence on the GMR effect. *J. Magn. Magn. Mater.* **258**–**259**, 338–341 (2003).

55. Lauter-Pasyuk, V. *et al.* Magnetic off-specular neutron scattering from Fe/Cr multilayers. *Phys. B Condens. Matter* **283**, 194–198 (2000).

Acknowledgements

Work support by NSF-DMR-1905277. A portion of this work was performed at the National High Magnetic Field Laboratory, which is supported by National Science Foundation Cooperative Agreement No. DMR-1644779 and the State of Florida. This research used resources at the Spallation Neutron Source, a Department of Energy Office of Science User Facility operated by the Oak Ridge National Laboratory. XRR measurements were conducted at the Center for Nanophase Materials Sciences (CNMS), which is a DOE Office of Science User Facility. We also acknowledge support from the Notre Dame Integrated Imaging Facility. This research used resources of the Advanced Photon Source, a U.S. Department of Energy (DOE) Office of Science User Facility, operated for the DOE Office of Science by Argonne National Laboratory under Contract No. DE-AC02–06CH11357.

Author contributions

JW, XL and BAA conceived the project. JW, MO and SKB carried out the magnetooptical experiments with input form BAA and DS. JW, HT and SKB analyzed the magnetooptical data. TW and JW carried out the k.p calculations. JW, ZZ and BAA carried out X-ray diffraction measurements. MZ and TO carried out TEM measurements. VL, HA and JK carried out and

analyzed neutron reflectivity and X-ray reflectivity measurements. XL synthesized the samples. JW, VL, XL and BAA interpreted the data from various experiments and wrote the manuscript.

Ethics declarations

The authors declare no competing interests.